2011/10/06
Head Id: 79712
Archive Id: 68987:79748M
Archive Date: 2011/09/28
Archive Tag: trunk

Measurement of the Production Cross Section of Pairs of Isolated Photons in pp collisions at $\sqrt{s} = 7\,\text{TeV}$

The CMS Collaboration

Abstract

The integrated and differential cross sections of the production of pairs of isolated photons have been measured in proton-proton collisions at a centre-of-mass energy of 7 TeV with the CMS detector at the LHC. Data corresponding to an integrated luminosity of 36 pb^{-1} have been analysed. A next-to-leading-order perturbative QCD calculation is compared to the measurements. A discrepancy is observed for regions of the phase space with small angle between the two emitted photons.

1 Introduction

The study of the production of energetic photon pairs in hadronic collisions is a valuable testing ground of the perturbative Quantum Chromodynamics (pQCD). The emission from hard parton-parton scattering of a pair of photons constitutes a particularly clean test of perturbation theory in the collinear- [1, 2] and k_{T} - [3] factorisation approaches, as well as of soft gluon logarithmic resummation techniques [4]. A comprehensive understanding of photon pair production is also important as it represents a major background to certain searches for rare or exotic processes, such as the production of a light Higgs boson, extra-dimension gravitons, and some supersymmetric states.

This paper presents a measurement of the production cross section of isolated photon pairs in proton-proton collisions at a centre-of-mass energy of $\sqrt{s} = 7$ TeV using the Compact Muon Solenoid (CMS) detector at the Large Hadron Collider (LHC). Photons produced in the hard scattering of quarks and gluons, called prompt, and isolated, are henceforth simply referred to as *signal photons* and the rest of the photons as *background photons*. A pair of signal photons will be referred to as a diphoton. The data sample was collected in 2010 and corresponds to an integrated luminosity of 36.0 pb^{-1}. Recent diphoton cross-section measurements have been performed by the D0 [5] and CDF [6, 7] collaborations, at the Tevatron proton-antiproton collider at $\sqrt{s} = 1.96$ TeV, and by the ATLAS collaboration at the LHC [8].

The CMS detector consists of a silicon pixel and strip tracker surrounded by a crystal electromagnetic calorimeter (ECAL) and by a brass-scintillator sampling hadron calorimeter (HCAL), all in an axial 3.8 T magnetic field provided by a superconducting solenoid of 6 m internal diameter. The gas-ionization detectors of the muon system are embedded in the steel return yoke of the magnet, in a field of 1.9 T. In addition to the barrel and endcap detectors, CMS has an extensive forward calorimetry system. A more detailed description of CMS can be found elsewhere [9].

In the CMS coordinate system, θ and φ respectively designate the polar angle with respect to the counterclockwise beam direction and the azimuthal angle, expressed in radians throughout this paper. The pseudorapidity is defined as $\eta = -\ln\tan\frac{\theta}{2}$.

The distance in the (η, φ) plane is defined as $R = \sqrt{(\Delta\eta)^2 + (\Delta\varphi)^2}$. The transverse energy E_{T} of a particle is defined as $E_{\mathrm{T}} = E\sin\theta$, where E is the energy of the particle. Its rapidity is defined as $y = \frac{1}{2}\ln\frac{E+p_z}{E-p_z}$, with p_z its longitudinal momentum with respect to the beam axis. Its transverse momentum is denoted p_T, $p_T = p\sin\theta$.

The electromagnetic calorimeter, which plays a major role in this measurement, consists of nearly 76 000 lead tungstate crystals. It is divided into a central part (barrel) covering the region $|\eta| < 1.48$ and a forward part (endcaps) extending the coverage up to $|\eta| < 3$ for a particle originating from the nominal interaction point. The crystals are arranged in a projective geometry with a granularity of 0.0174 in both the η and φ directions in the barrel, and increasing with η from 0.021 to 0.050 in the endcaps. A preshower detector consisting of two planes of silicon sensors interleaved, with a total radiation lenght $3X_0$ of lead, is placed in front of the endcaps to cover the pseudorapidity region $1.65 < |\eta| < 2.6$.

The differential cross section is measured as a function of variables which are particularly relevant in searches for rare processes or to characterise QCD interactions (see e.g. [2]):

- the diphoton invariant mass, $m_{\gamma\gamma}$;
- the azimuthal angle between the two photons, $\Delta\varphi_{\gamma\gamma}$;

- the transverse momentum of the photon pair, $p_{T,\gamma\gamma} = \sqrt{{p_{T,\gamma_1}}^2 + {p_{T,\gamma_2}}^2 + 2\, p_{T,\gamma_1} p_{T,\gamma_2} \cos\Delta\varphi_{\gamma\gamma}}$, where p_{T,γ_1} and p_{T,γ_2} are the magnitudes of the transverse momenta of the two photons;
- and $\cos\theta^* = \tanh\frac{\Delta y_{\gamma\gamma}}{2}$, $\Delta y_{\gamma\gamma}$ being the difference between the two photon rapidities. At lowest order, θ^* is the center-of-mass scattering angle of $q\bar{q} \to \gamma\gamma$ and $gg \to \gamma\gamma$ processes.

In addition, the integrated cross section is measured. The measurements refer to a kinematic acceptance requiring at least one isolated photon with $E_\mathrm{T} > 23\,\mathrm{GeV}$ and a second isolated photon with $E_\mathrm{T} > 20\,\mathrm{GeV}$, separated by $R > 0.45$. They are performed in two pseudorapidity regions, one with $|\eta| < 1.44$, and the other with $|\eta| < 2.5$ but excluding the transition region between the barrel and endcap calorimeters, $1.44 < |\eta| < 1.57$. For convenience the latter will be referred to as $|\eta| < 2.5$ throughout the paper.

Asymmetric thresholds were applied on the photon transverse momenta to avoid the infrared sensitivity affecting the fixed-order calculation [10, 11] and ease the comparison of the measurement with the theoretical prediction.

All simulations results are based on the PYTHIA 6.4.22 [12] event generator, Z2 tune [13], CTEQ6L PDF [14], and a GEANT 4 modelling of the detector. In simulation a prompt photon is considered as signal if the sum of the transverse momenta of the particles within a cone $R < 0.4$ around the photon direction is less than $5\,\mathrm{GeV}$.

Event selection and background discrimination are presented in Sections 2 and 3. The determination of the signal yield and the measurement of the cross-section will be explained in the Sections 4 and 5. Results are discussed in the Section 8 and compared with the theoretical predictions introduced in Section 7.

2 Event Selection

Photon candidates in CMS are reconstructed by clustering the energy deposited in the ECAL crystals [15, 16]. CMS is equipped with a versatile trigger to adapt to the LHC luminosity ramp-up. In this measurement three trigger settings were used for three successive data taking periods. They require two photon candidates, with a threshold of either $15\,\mathrm{GeV}$ or $17\,\mathrm{GeV}$ on the transverse momentum of both candidates. For the last period, with the highest instantaneous luminosity, a weak isolation requirement was applied on one of the two photon candidates. For the three periods, the trigger efficiency for events passing the analysis selections described in the following paragraphs is estimated from simulated events to be greater than 99.9%. The offline event selection requires one photon candidate with $E_\mathrm{T} > 23\,\mathrm{GeV}$ and a second photon candidate with $E_\mathrm{T} > 20\,\mathrm{GeV}$, each within the ECAL fiducial region (detector region covering $|\eta| < 1.44$ and $|\eta| > 1.57$) and within the tracker acceptance (detector region covering $|\eta| < 2.5$). The candidates are required to be separated by $R > 0.45$ to avoid overlap between their isolation region.

Photon identification criteria requiring the deposits in the calorimeters to be compatible with an electromagnetic shower are applied on the two candidates. The criteria are based on the spread along η of the energy clustered in the ECAL, henceforth referred to as $\sigma_{i\eta\, i\eta}$, and on the ratio H/E of the energy measured in HCAL and ECAL (see *loose selections* in Ref. [16]).

The photon candidates are required to be isolated. The sum of the transverse momenta of charged particles measured by the tracker and the sum of the transverse energy deposits in

HCAL, both defined within a cone of radius $R = 0.4$ around the photon direction, must each be less than 2 GeV in the barrel and 4 GeV in the endcaps. HCAL deposits in a cone of radius $R = 0.15$ are excluded from the sum as well as tracks in a cone of radius $R = 0.04$ and within a strip of $\Delta\eta = 0.03$ along the φ direction, which can potentially contain tracks of an electron-positron pair from a conversion of the photon in the tracker material. The sum of the transverse energy deposited in ECAL in a cone of radius $R = 0.3$ is required to be less than 20% of the photon transverse energy, in order to be consistent with the trigger requirements applied online. Excluded from the sum is the energy deposited within a cone of a radius corresponding to 3.5 crystals along η and within a 5-crystal-wide strip along φ. In addition, it is required that no charged particle with the following properties impinges on ECAL within a cone of radius $R = 0.4$: $p_{\mathrm{T}} > 3\,\mathrm{GeV}$, impact parameters with regard to the primary vertex in the transverse and longitudinal planes of less than 1 mm and 2 mm, respectively, and associated with a hit in the innermost layer of the pixel detector. Tracks corresponding to such particles are henceforth called *impinging tracks*. The electron contamination is further reduced by imposing an additional veto on the presence of hits in the layers of the pixel detector along the direction of the photon candidate.

3 Signal and Background Discrimination

After selection, candidate photons are either signal photons, background photons coming from hadron decays, the larger component coming from neutral meson decaying into a pair of collinear photons which is misidentified as a single one, or misidentified electrons. The backgrounds to diphotons are photon-jet and multi-jet events, with respectively one and two background photons from neutral hadron decays, and Drell-Yan events, with two misidentified electrons.

The remaining contamination from Drell-Yan events is estimated from simulation using the next-to-leading order (NLO) POWHEG generator [17–19], which reproduces well our own measurement [20]. The diphoton cross-section measurement is corrected for this contamination, which amounts to about 12% in the mass range $80 - 100\,\mathrm{GeV}$ around the Z peak. This procedure has a negligible impact on the systematic uncertainties.

Background photons from photon-jet and multi-jet events leave a wider footprint in ECAL than signal photons and are produced in jets alongside other particles, which also deposit energy in ECAL. An isolation variable $\mathcal{I}$ based on the energy in the electromagnetic calorimeter is used to statistically estimate the fraction of diphoton events among the selected candidates. This variable is constructed to minimise the dependence on the energy deposited by minimum-ionising particles (MIPs) such that its distribution for the background can be obtained from data,the impinging-track method described thereafter, and it differs from the loose ECAL isolation used in the selection (see Section 2). It is defined as the sum of the transverse energy of the ECAL deposits with $E_{\mathrm{T}} > 300$ MeV (MIPs veto), within a hollow cone centred on the photon impact point, of inner radius of 3.5 crystal edges and outer radius of $R = 0.4$. Deposits assigned to the photon itself or falling within a 5-crystal-wide strip along φ are removed. Thus, deposits from photons converting into electron-positron pairs in the tracker material being spread along φ do not contribute to the value of the electromagnetic isolation.

Since the distribution of $\mathcal{I}$ is different for signal photons and background photons, this variable can be used in a maximum likelihood fit to extract the number of signal events in the entire selected sample. Fig. 1 shows the probability density function of $\mathcal{I}$, which was extracted from data with the methods described in the following.

Contributions to the value of the ECAL isolation variable for signal photons come from pile-up and underlying event activity. These contributions being independent of φ, the ECAL isolation probability density function $f(\mathcal{I})$ is estimated from *random cones* using events with at least one isolated photon candidate. The isolation variable $\mathcal{I}$ is calculated in a cone of $R = 0.4$ around an axis at the same η as the photon candidate and at a random φ in a $\pi/2$ window around the axis perpendicular to the photon direction. The cone is also required not to include photon and electron candidates or jets. The ECAL isolation probability density function for signal photons is cross-checked with two additional independent methods, both exploiting e^+ and e^-, from Z and W boson decays, that do not radiate significantly in the tracker material, selected with a constraint on the fraction of bremsstrahlung energy emitted from the interaction in the tracker material is imposed. Such electrons and positrons leave ECAL energy deposits compatible with those of photons, and have a similar probability density function for $\mathcal{I}$. The $Z \to e^+e^-$ events are selected with stringent requirements on the identification criteria of the lepton pair and on its invariant mass and the $f(\mathcal{I})$ distribution is obtained directly from both leptons. In $W \to e\nu$ events, $f(\mathcal{I})$ is obtained by exploiting the *sPlot* technique [21]. The missing transverse energy projected along the lepton axis is used to estimate the probability of an event to be signal ($W \to e\nu$) or background ($Z \to e^+e^-$, $W \to \tau\nu$, $\gamma +$ jet(s), QCD multijet processes) and the value of $\mathcal{I}$ of the selected candidates is weighted accordingly, to estimate the distribution of $\mathcal{I}$. The uncertainty on $f(\mathcal{I})$ is taken to be the maximum difference between the distributions extracted from random cones and from electrons in Z and W events. In simulated events, the difference between $f(\mathcal{I})$ for signal photons and for random cones is lower than the uncertainty determined from data.

For background photons, $f(\mathcal{I})$ is extracted from a background sample with less than 0.1% of signal photons contamination. The sample is obtained by selecting photon candidates with one and only one impinging track. A cone of $R = 0.05$ around the track is excluded from the isolation area to avoid counting the energy deposited by the charged particle. The isolation variable $\mathcal{I}$ is then normalised to the nominal isolation area. To validate this method, a distribution of $\mathcal{I}$ is also extracted from a sample of events with two impinging tracks, one of the two being excluded in the computation of $\mathcal{I}$. The latter distribution is compared to the one obtained on the one-impinging-track sample, using the normal definition of $\mathcal{I}$, i.e. including the energy

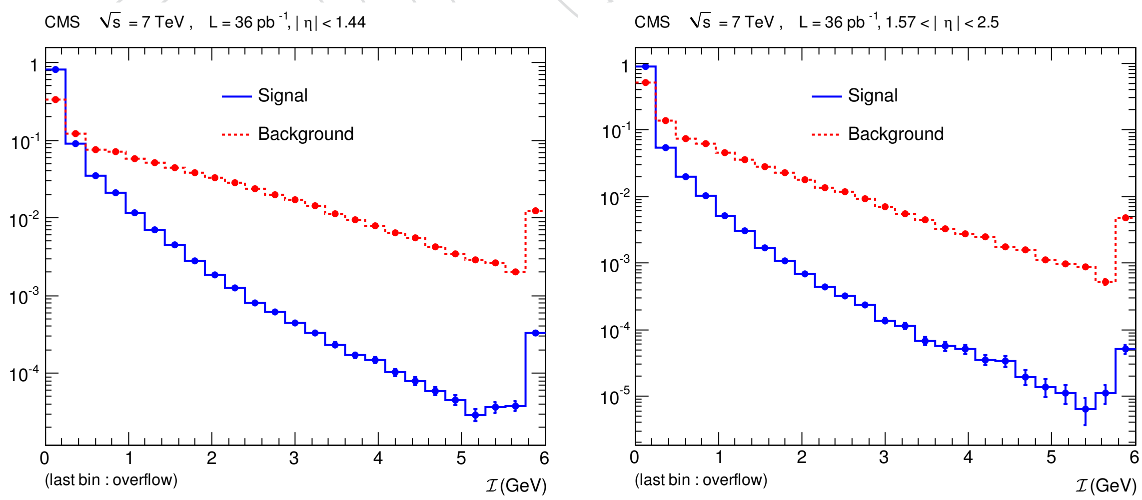

(a) (b)

Figure 1: Probability density functions of $\mathcal{I}$ for signal photons (blue) and background photons (dashed red) in the barrel (left) and in the endcap (right).

deposits in the vicinity of the track. The agreement is within one sigma in the entire range of the $\mathcal{I}$ distribution and the difference is taken as a systematic uncertainty on the knowledge of $f(\mathcal{I})$ for background photons.

The distributions $f(\mathcal{I})$ show a moderate dependence on η and on the pile-up conditions, quantified by the number n_{vtx} of primary vertices in the events (2.4 on average). The background distribution $f(\mathcal{I})$ depends also on the transverse energy E_{T} of the candidate. Therefore, events in the sample used for the extraction of $f(\mathcal{I})$ are weighted to reproduce the distributions of η, n_{vtx}, and E_{T} of the diphoton sample. The approximation made by using the diphoton sample in place of the signal and background distributions is taken into account in the systematic uncertainties. The distributions $f(\mathcal{I})$ for signal and background photons used in the maximum likelihood fit are shown in Fig. 1.

4 Signal Yield Determination

The number of diphoton events is obtained from a maximum-likelihood fit to the distributions of the ECAL isolation variables of the two photons, $\mathcal{I}_1$ and $\mathcal{I}_2$, where numbers 1 and 2 are assigned randomly. Events are separated into three types: signal events ($\gamma\gamma$) if both photons are signal photons, background events with a signal photon and a background photon, and background events with two background photons.

The likelihood function $\mathcal{L}$ maximised in the fit is

$$\mathcal{L} = \frac{e^{-N^{\mathrm{tot}}}}{N!} \prod_{i=1}^{N} \sum_{t \in \mathcal{T}} N_t f_t(\mathcal{I}_1^i, \mathcal{I}_2^i) \,, \tag{1}$$

where $\mathcal{T}$ indicates the three event types, N is the event sample size, N_t are the numbers of events estimated in the fit for each type t, N^{tot} is their sum over the three event types, and $f_t(\mathcal{I}_1, \mathcal{I}_2)$ is the probability for the ECAL isolation variables of the two photons to have values $\mathcal{I}_1$ and $\mathcal{I}_2$ for the given event type t.

The probability density functions for the three event types are obtained by multiplying the probability density functions $f(\mathcal{I})$ for single photon candidates assuming the two statistical variables $\mathcal{I}_1$ and $\mathcal{I}_2$ to be independent. Correlations between these two variables have been checked with simulation and are small enough to be neglected.

The requirements described in Section 2 select 5977 events. These events are divided into three subsamples depending on whether both photons are in the barrel (2191 events), one is in the barrel and the other in the endcaps (2527 events), or both are in the endcaps (1259 events). The fit is performed separately for each of the three subsamples in each bin of each observable. An example of the fit for one bin of $m_{\gamma\gamma}$ spectrum is shown in Fig. 2 for events with both photons in the barrel ($|\eta| < 1.44$).

The maximum likelihood method is known to be biased for samples with small numbers of events. This bias is estimated with Monte-Carlo pseudo-experiments and the result of the fit corrected for it. It is less than 10% of the statistical error in 80% of the bins and never exceeds half the statistical error.

5 Cross-Section Measurement

The differential cross-section measurements $d\sigma/dX$, for the variable X in the interval X_i reads

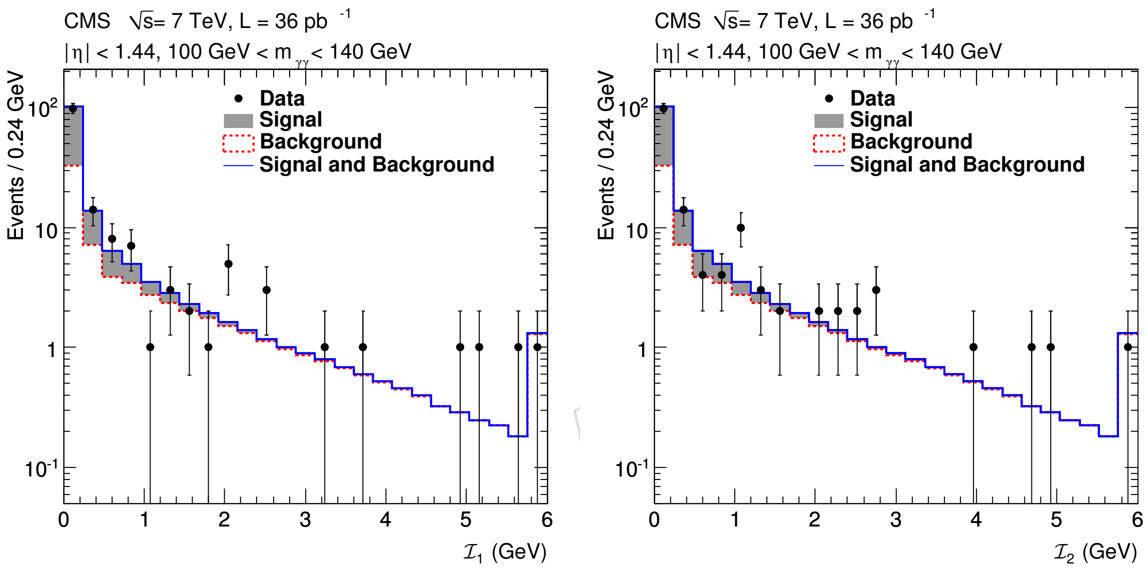

(a) (b)

Figure 2: Fit of the photon ECAL isolation $(\mathcal{I}_1, \mathcal{I}_2)$ in the bin $100\,\mathrm{GeV} < m_{\gamma\gamma} < 140\,\mathrm{GeV}$ for photons with $|\eta| < 1.44$. The distribution of the isolation variable $\mathcal{I}_1$ of one photon candidate, arbitrarily chosen as "first photon" and denoted with subscript '1', is represented on the left figure together with the fit result, integrated over $\mathcal{I}_2$: the dashed line represents the background contribution while the continuous line the sum of the signal and background contributions. The same distributions for the second photon candidate is represented on the right figure. In this mass bin, with 161 selected candidates, the number of signal events is 72 ± 14.

$$\frac{d\sigma}{dX}(X_i) = \frac{N^{\mathrm{U}}_{\gamma\gamma}(X_i)}{\mathcal{L}\Delta X_i \mathcal{C}(X_i)}\,, \tag{2}$$

where $N^{\mathrm{U}}_{\gamma\gamma}$ is the number of signal events unfolded for the detector resolution and corrected for the Drell-Yan contamination, $\mathcal{L}$ the total integrated luminosity, ΔX_i the interval width, and $\mathcal{C}$ a correction factor for the effects of the finite detector resolution on the acceptance and on the efficiencies of photon reconstruction and identification.

The number of signal events is unfolded for the detector resolution by inverting the response matrix T obtained from simulated events passing the selection requirements for $m_{\gamma\gamma}$, $p_{T,\gamma\gamma}$, $\Delta\varphi_{\gamma\gamma}$, and $|\cos\theta^*|$. The matrix elements T^{ik} are the probabilities of a selected event with the generated value of X in bin X_k to be reconstructed with a value of X in bin X_i. For a given interval X_i, the number of events after unfolding is related to the observed numbers of events in the different intervals X_k by: $N^{\mathrm{U}}_{\gamma\gamma}(X_i) = \left(T^{ik}\right)^{-1} N_{\gamma\gamma}(X_k)$. Here, $N_{\gamma\gamma}(X_k)$ is the signal yield corrected for the Drell-Yan contamination as described in Sec. 3. Given the excellent performance of ECAL, the matrix is nearly diagonal and no regularisation is applied in the unfolding procedure. The unfolding effect is below 5% for all distributions and bins, except in the bins around the local peaks of the diphoton mass and p_T distributions, where it is of the order of 15%.

The correction factor $\mathcal{C}(X_i)$ is defined as

$$\mathcal{C}(X_i) = \frac{N^{\mathrm{sim}}_{\mathrm{reco}}(X_i)}{N^{\mathrm{sim}}_{\mathrm{gen}}(X_i)}\frac{\varepsilon^{\mathrm{data}}}{\varepsilon^{\mathrm{sim}}}, \tag{3}$$

where

$N^{\mathbf{sim}}_{\mathbf{reco}}(X_i)$ is the number of simulated events passing all the selection criteria, with generated value of X within the interval X_i;

$N^{\mathbf{sim}}_{\mathbf{gen}}(X_i)$ is the number of simulated events within the acceptance defined at generator level (Section 1), with generated values of X within the interval X_i;

$\varepsilon^{\mathbf{data}}$ is the efficiency of the photon identification criteria measured from data;

$\varepsilon^{\mathbf{sim}}$ is the efficiency of the photon identification criteria obtained on simulated events using the same technique as for $\varepsilon^{\mathrm{data}}$.

The efficiencies $\varepsilon^{\mathrm{data}}$ and $\varepsilon^{\mathrm{sim}}$ to observe a diphoton candidate are taken as the square of the efficiencies to observe a single photon.

The efficiency for the requirements on isolation, $\sigma_{i\eta\, i\eta}$, and H/E is estimated with a tag-and-probe method" [22] applied to a $Z \to e^+e^-$ sample selected from the full CMS dataset collected in 2010. One lepton, the tag, is selected with tight reconstruction and identification criteria [23], while the other, the probe, is selected by requiring a constraint on the invariant mass of the lepton pair. The probes constitute a sample of unbiased electrons and positrons. The same constraint as the one discussed in Section 3 is applied on the fraction of bremsstrahlung energy emitted by the e^+ and e^- from the interaction in the tracker material. This ensures that the electromagnetic deposits of these "low-radiating" electrons and positrons are compatible with those of a photon shower. The efficiency is computed by applying the requirements on isolation, $\sigma_{i\eta\, i\eta}$, and H/E to this sample and is given by the fraction of probes passing the selection.

The efficiency for the requirement to have no impinging tracks within the isolation cone is estimated from data, using a control sample built using a *random-cone* technique on events with a single photon selected according to the identification criteria described above. The random cone definition is the one introduced as in Section 3 for the extraction of $f(\mathcal{I})$. Particles within the random cone hence come mainly from pile-up and the underlying event. Therefore, quantities such as the number of impinging tracks or energy deposits in the isolation area are assumed to be the same as for isolated photons. The efficiency of the requirement to have no impinging track within the isolation cone is given by the ratio of random cones passing this criteria to the total number of random cones. The efficiency of the veto on pixel hits is obtained from simulation. It is included in the $N^{\text{sim}}_{\text{reco}}/N^{\text{sim}}_{\text{gen}}$ term of expression (3).

The correction factor $\mathcal{C}$ is 80.8 $\pm$ 1.9% for the total cross section in the region $|\eta| < 1.44$, and 76.2 $\pm$ 3.3% in the region $|\eta| < 1.44$ or $1.57 < |\eta| < 2.5$.

6 Systematic Uncertainties

The uncertainties on the reconstruction of the photon four-momentum are dominated by the ECAL energy scale, known at the level of 0.6 % in the barrel and of 1.5 % in the endcaps [24]. This affects the definition of the acceptance and induces bin-to-bin migrations in the differential cross sections. The former impacts only kinematics regions near the photon p_T thresholds and results in an uncertainty of 40% in the most affected region, the lowest masses of $d\sigma/dm_{\gamma\gamma}$. The uncertainty from the bin-to-bin migration is about 1%.

The uncertainties associated with the photon identification efficiency include the statistical and systematic uncertainties added in quadrature. For the tag-and-probe and random-cone methods, the systematic uncertainty is estimated by applying the respective methods on simulated data: the difference between the value obtained with the method and the value given by the fraction of simulated events passing the identification criterion is taken as systematic uncertainty. This estimate is conservative, considering that the efficiency calculation includes already a correction for this difference. The total uncertainties are 1.9 % for diphotons in the barrel and 3.3 % for all diphotons.

Table 1: Different contributions to the systematic uncertainties on the measured differential cross sections The systematic uncertainties are computed for each bin of Figures 3 to 10. In this table is listed the typical value over the different bins.

Uncertainty source	$\|\eta\| < 1.44$	$\|\eta\| < 1.44$ or $1.57 < \|\eta\| < 2.5$
Energy scale on acceptance	1.5%	2%
Energy scale on bin-to-bin migration	1%	1.5%
Signal and background distribution, $f(\mathcal{I})$	7%	9%
Acceptance and efficiency correction factor, $\mathcal{C}$	2%	3%
Luminosity	4.0%	4.0%
Total	8%	11%

The impact of imperfect knowledge of the signal and background distributions $f(\mathcal{I})$ is estimated with Monte Carlo pseudo-experiments where $f(\mathcal{I})$ are varied. The extent of the variations corresponds to the discrepancies between the shapes of the principal and cross-check distributions observed in the validation of the random-cone and impinging-track methods (Section 3). In the first bin of the probability density functions, they are of the order of ± 0.01 for the signal and range from ± 0.03 to ± 0.05 for the background. The uncertainty on the $f(\mathcal{I})$ estimation from its dependence on the distribution of photon transverse momentum p_T, photon pseudorapidity η, and number of vertices n_{vtx} is estimated by considering the change on $f(\mathcal{I})$ observed when using the p_T, η, and n_{vtx} distributions obtained from the diphoton simulation instead of the ones from the diphoton event candidates. The effect of the latter on the measurement is negligible. The overall impact of the knowledge of the signal and background distributions on the integrated cross section is $\sim$ 8%, and varies from 4 to 27% on differential cross sections, depending on the bin and the subsample.

A 4% uncertainty is assigned to the integrated luminosity corresponding to the dataset [25]. The various contributions to the systematic uncertainties are summarised in Table 1.

7 Theoretical Predictions

This Section introduces the theoretical calculations which are compared against the experimental data in Section 8. The leading contributions to the production of pairs of prompt photons in pp collisions are the quark-antiquark annihilation ($q\bar{q} \to \gamma\gamma$), gluon fusion ($gg \to \gamma\gamma$), and gluon-(anti)quark scattering ($qg \to \gamma\gamma q$) processes. One or both photons come either directly from the hard process or from a parton fragmentation, a cascade of successive collinear splittings ending up with a radiated photon. Contributions from the quark annihilation process and the single and double fragmentation processes are calculated up to order $\alpha_s\alpha^2$ with the DIPHOX 1.3.2 program [1]. The contributions from the gluon-fusion process $gg \to \gamma\gamma$, including the one-loop box of order $\alpha_s^2\alpha^2$, the interference between the one- and two-loop boxes, and the real emission one-loop "pentagon" $gg \to \gamma\gamma g$, both of order $\alpha_s^3\alpha^2$, are calculated with the GAMMA2MC 1.1.1 program [2]. The fragmentation function BFG set II [26] has been used in the calculation. Although being higher-order processes, the gluon-fusion contributions are quantitatively comparable to those from quark-antiquark annihilation in the mass range of interest (including the region pertinent to the $H \to \gamma\gamma$ search), due to the significant gluon luminosity in this range at the LHC. The three theoretical scales, normalisation, initial factorisation, and fragmentation, are set to the diphoton mass value.

The photons are required to be within the kinematic acceptance defined in Section 1. An additional isolation requirement at the parton level is imposed by requiring the total hadronic transverse energy deposited in a cone of radius 0.4 centred on the photon to be less than 5 GeV. Particles resulting from underlying event activity and hadronisation are not included in partonic event generators such as DIPHOX and GAMMA2MC. The fraction of diphotons not selected due to underlying hadronic activity falling inside the isolation cone is estimated using the PYTHIA 6.4.22 [12] event generator with the tunes D6T [27], Z2 [13], P0 [28], and DWT [27]. The parton-level cross section is corrected by a factor 0.95 ± 0.04.

The uncertainties associated with the limited knowledge of the parton distribution functions (PDFs) and the strong coupling constant α_s are determined according to the PDF4LHC recommendations [29]. The cross section is computed with three different PDF sets (CT10 [30], MSTW08 [31], and NNPDF21 [32]) taking into account their associated uncertainties and the uncertainties on α_s. The respective preferred α_s central value of the PDF sets is used and α_s is varied within ± 0.012. The value for the cross section is taken as the mid-point of the envelope of the three results, including the errors. The error on the cross section is taken to be the

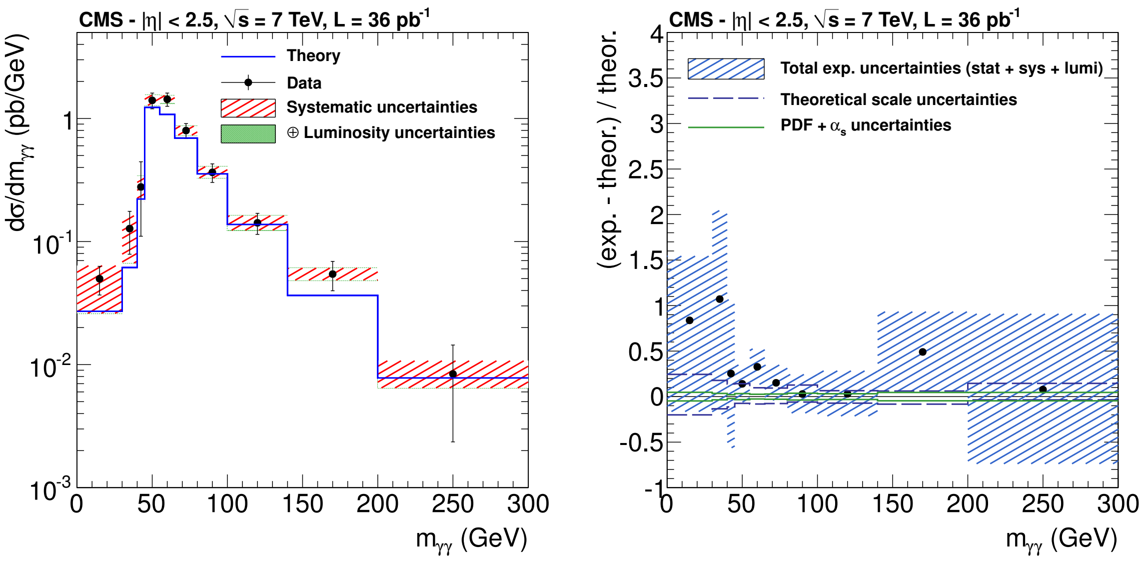

(a) (b)

Figure 3: Measured cross section of diphoton production as (a) a function of the invariant mass of the photon pair and (b) bin-by-bin comparison with the theory for photons within the pseudorapidity region $|\eta| < 1.44$ or $1.57 < |\eta| < 2.5$. The total systematic uncertainties are represented by the shaded area, the different contributions are added in quadrature sequentially.

envelope.

The theoretical scale uncertainties are estimated by varying the normalisation, initial factorisation, and fragmentation scales by factors of 1/2 and 2, keeping the ratio between two scales less than 2 (for instance the combination $0.5\,m_{\gamma\gamma}$, $2\,m_{\gamma\gamma}$, $m_{\gamma\gamma}$ is not considered). The uncertainty is taken to be the maximum difference in the obtained cross sections.

8 Results

The integrated cross sections obtained for the acceptance defined in Section 2 are:

$$\begin{aligned}
\sigma(pp \to \gamma\gamma)|_{|\eta|<1.44} &= 31.0 \ \pm 1.8\,(\text{stat}) \ {}^{+2.0}_{-2.1}\,(\text{syst}) \ \pm 1.2\,(\text{lumi}) \ \text{pb}\,, \\
\sigma(pp \to \gamma\gamma)|_{|\eta|<2.50} &= 62.4 \ \pm 3.6\,(\text{stat}) \ {}^{+5.3}_{-5.8}\,(\text{syst}) \ \pm 2.5\,(\text{lumi}) \ \text{pb}.
\end{aligned}$$

The calculation performed as described in previous section predicts,

$$\begin{aligned}
\sigma(pp \to \gamma\gamma)|_{|\eta|<1.44} &= 27.3 \ {}^{+3.0}_{-2.2}\,(\text{scales}) \ \pm 1.1\,(\text{PDF}) \ \text{pb}\,, \\
\sigma(pp \to \gamma\gamma)|_{|\eta|<2.50} &= 52.7 \ {}^{+5.8}_{-4.2}\,(\text{scales}) \ \pm 2.0\,(\text{PDF}) \ \text{pb}.
\end{aligned}$$

The integrated cross-sections obtained from the calculation are compatible with the measurements within the experimental and theoretical uncertainties.

The differential cross-section measurements for the two considered pseudorapidity ranges are shown along with the theoretical predictions in Figures 3 through 10. The values of the cross sections for each bin are provided in Tables 2 to 5. As can be seen in Fig. 7 and Fig. 8, the prediction underestimates the measured cross section for $\Delta\varphi_{\gamma\gamma} < 2.8$. In the leading-order (LO) term of gluon fusion and quark annihilation $2 \to 2$ processes, the two photons are back-to-back because of momentum conservation. Therefore the LO term does not contribute to this

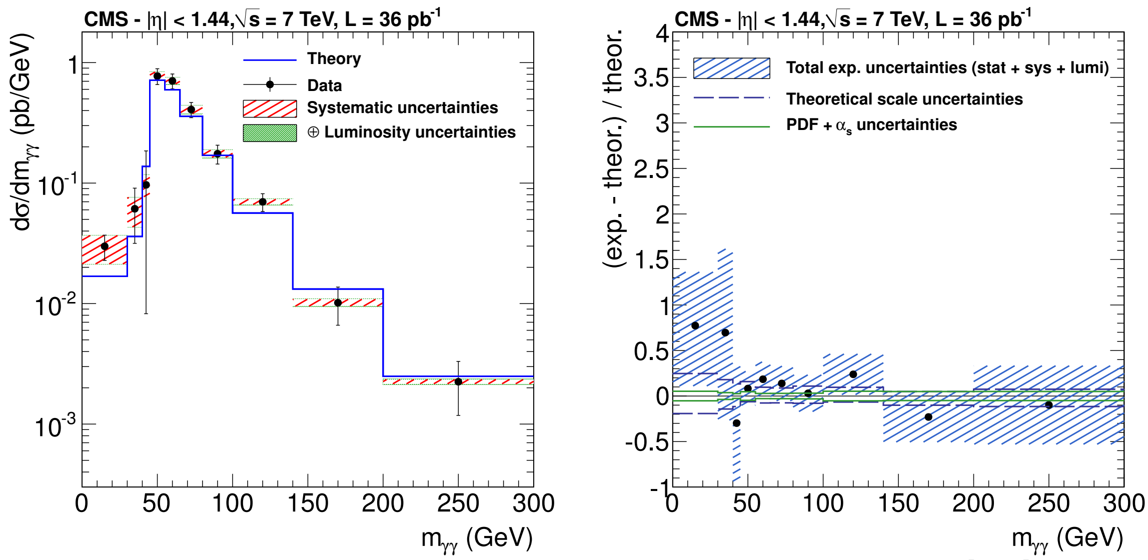

(a)

(b)

Figure 4: Measured cross section of diphoton production (a) as a function of the invariant mass of the photon pair and (b) bin-by-bin comparison with the theory for photons within the pseudorapidity region $|\eta| < 1.44$. The total systematic uncertainties are represented by the shaded area, the different contributions are added in quadrature sequentially.

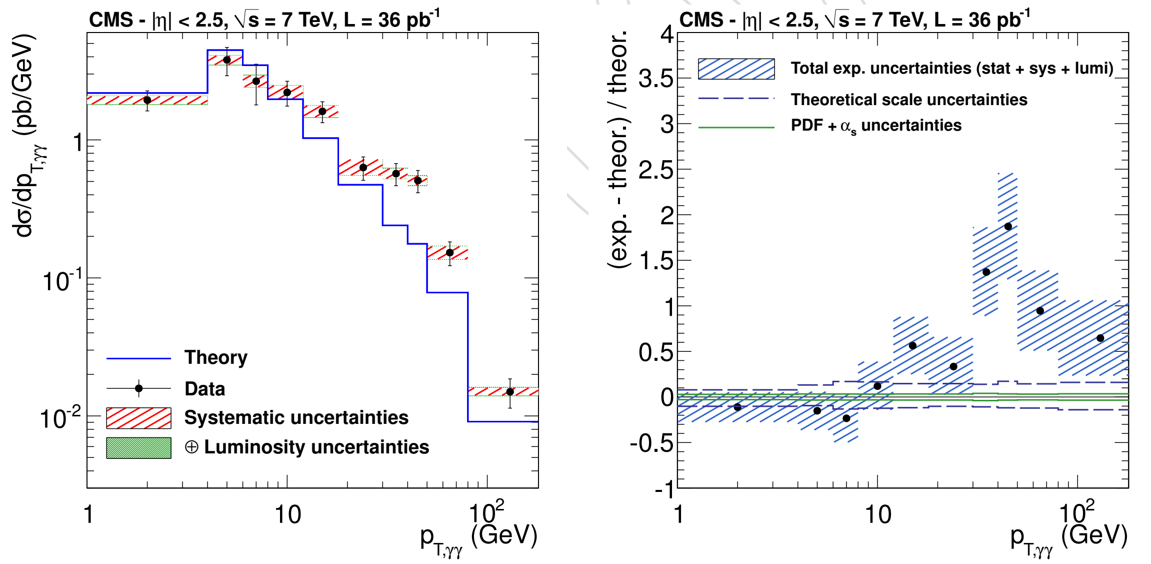

(a)

(b)

Figure 5: Measured cross section of diphoton production (a) as a function of the transverse momentum of the photon pair and (b) bin-by-bin comparison with the theory for photons within the pseudorapidity region $|\eta| < 1.44$ or $1.57 < |\eta| < 2.5$. The total systematic uncertainties are represented by the shaded area, the different contributions are added in quadrature sequentially.

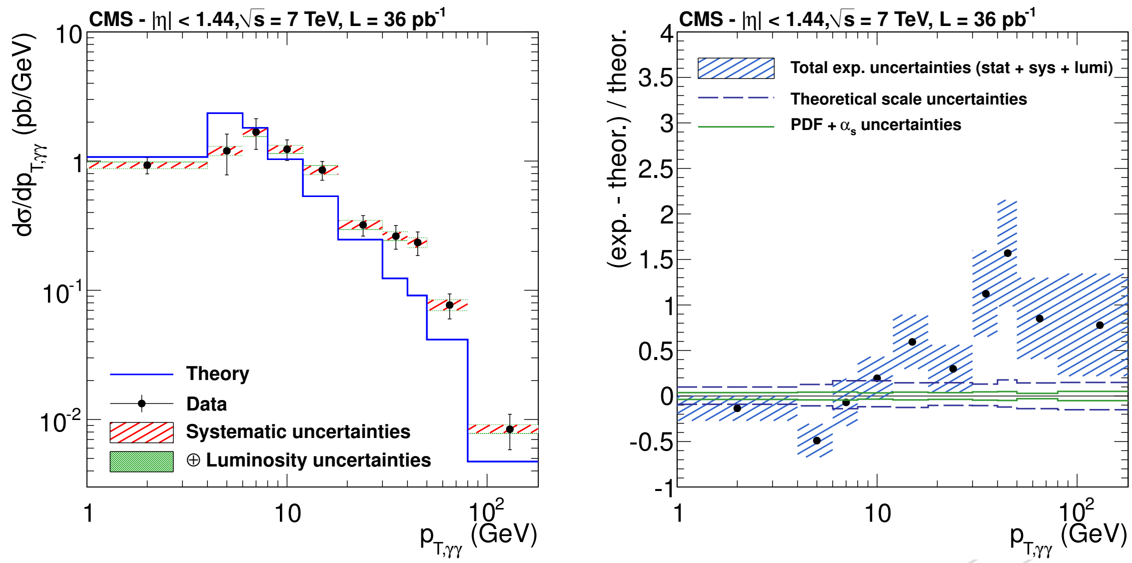

(a) (b)

Figure 6: Measured cross section of diphoton production (a) as a function of the transverse momentum of the photon pair and (b) bin-by-bin comparison with the theory for photons within the pseudorapidity region $|\eta| < 1.44$. The total systematic uncertainties are represented by the shaded area, the different contributions are added in quadrature sequentially.

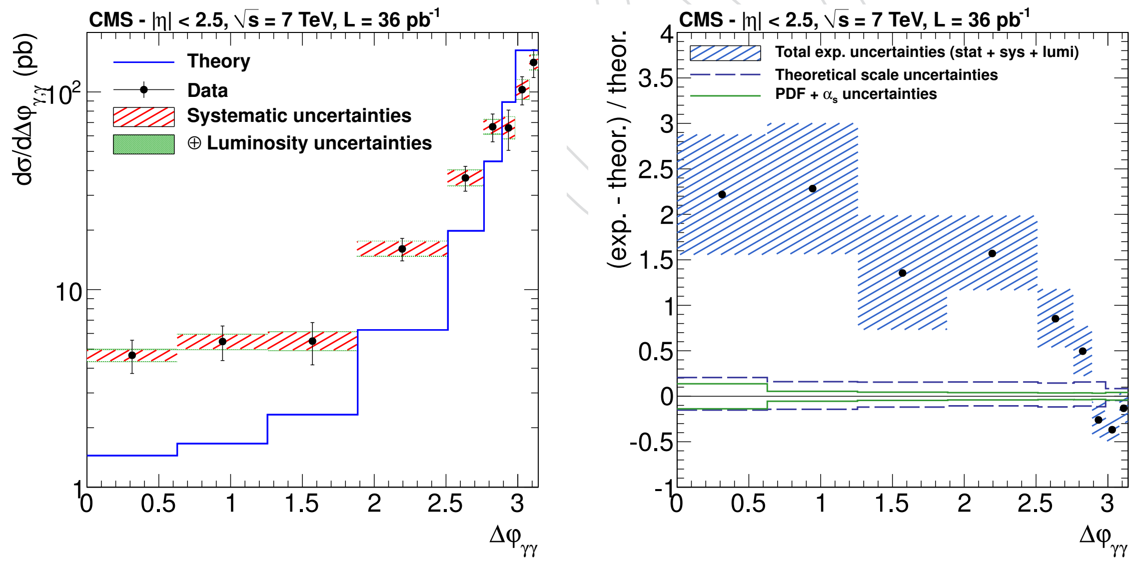

(a) (b)

Figure 7: Measured cross section of diphoton production (a) as a function of the azimuthal angle between the two photons and (b) bin-by-bin comparison with the theory (b) for photons within the pseudorapidity region $|\eta| < 1.44$ or $1.57 < |\eta| < 2.5$. The total systematic uncertainties are represented by the shaded area, the different contributions are added in quadrature sequentially.

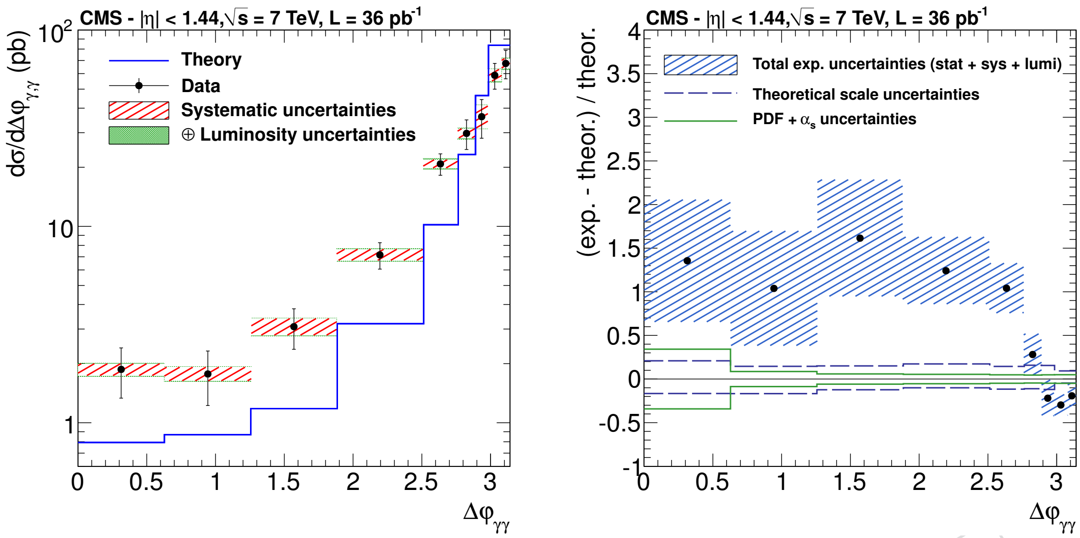

(a) (b)

Figure 8: Measured cross section of diphoton production (a) as a function of the azimuthal angle between the two photons and (b) bin-by-bin comparison with the theory for photons within the pseudorapidity region $|\eta| < 1.44$. The total systematic uncertainties are represented by the shaded area, the different contributions are added in quadrature sequentially.

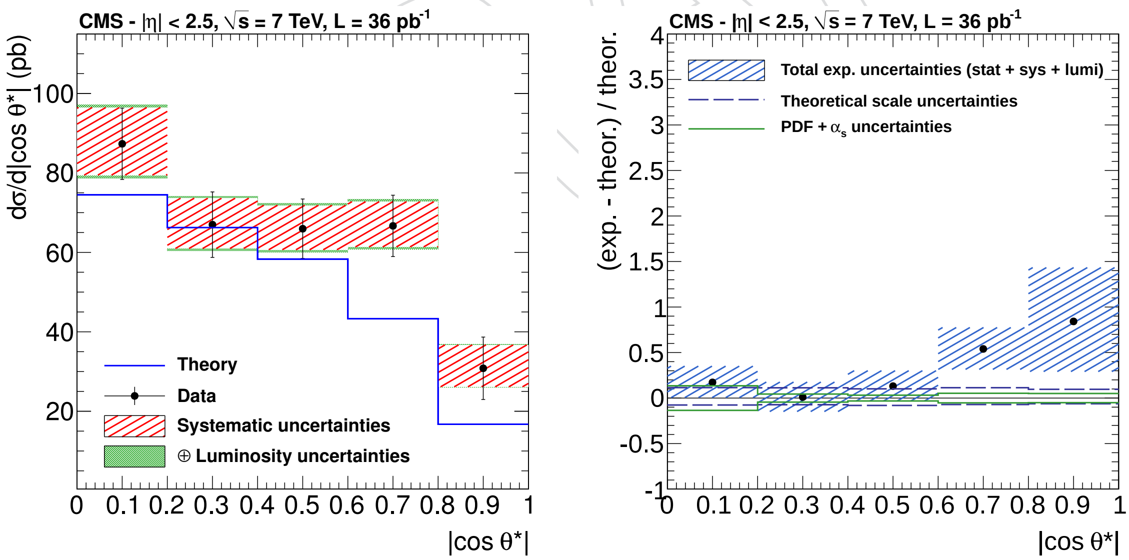

(a) (b)

Figure 9: Measured cross section of diphoton production (a) as a function of $cos\theta* = tanh\frac{y}{2}$ and (b) bin-by-bin comparison with the theory for photons within the pseudorapidity region $|\eta| < 1.44$ or $1.57 < |\eta| < 2.5$. The total systematic uncertainties are represented by the shaded area, the different contributions are added in quadrature sequentially.

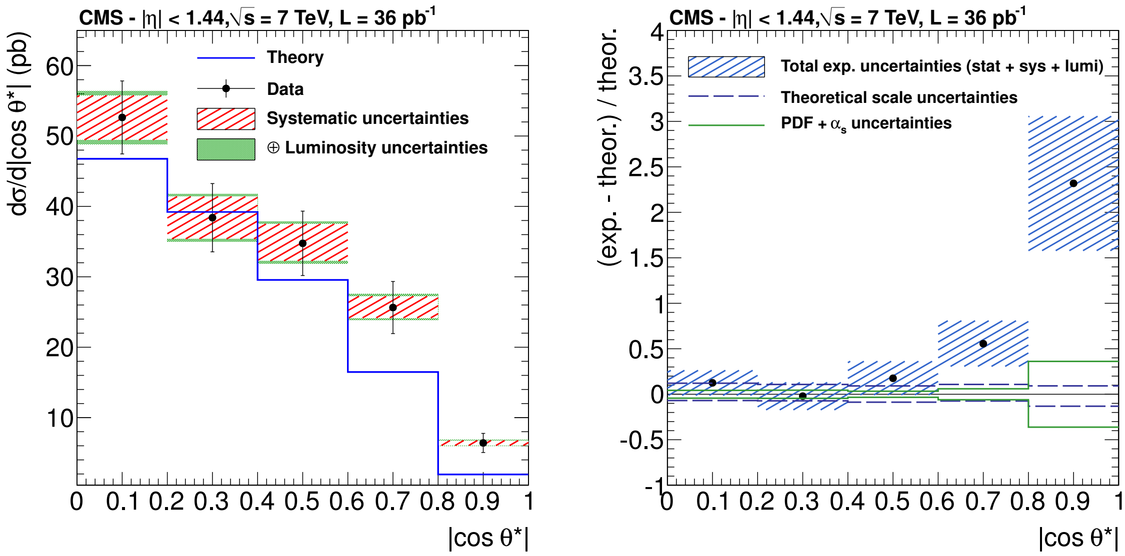

(a) (b)

Figure 10: Measured cross section of diphoton production as (a) a function of $cos\theta* = tanh\frac{y}{2}$ and (b) bin-by-bin comparison with the theory for photons within the pseudorapidity region $|\eta| < 1.44$. The last bin of the histogram, $0.8 < |\cos\theta^*| < 1$, is only populated up to $|\cos\theta^*| < 0.95$, limit resulting from the $|\eta|$ boundary. The total systematic uncertainties are represented by the shaded area, the different contributions are added in quadrature sequentially.

phase space region, which is effectively covered in the NLO calculation by only one order for both direct and fragmentation production. The contribution for $\Delta\varphi_{\gamma\gamma} \lesssim \pi$, combined with the requirements of $E_T > 20, 23\,\text{GeV}$ on the two photons, is responsible for the shoulder in the vicinity of 40 GeV observed in the diphoton E_T distribution of Fig. 5 and Fig. 6. This contribution also populates the region below 30 GeV in the diphoton mass distribution shown in Fig. 3 and Fig. 4. In these two regions of the $p_{T,\gamma\gamma}$ and $m_{\gamma\gamma}$ spectra, the calculated cross section is lower than the measurement, consistently with the deficit for $\Delta\varphi_{\gamma\gamma} < 2.8$. This disagreement provides valuable input for the calculation of processes not covered by current theoretical predictions.

Comparison of the measurements of the $\cos^* = \tanh y2$ spectrum shown Fig. 9 and Fig. 9 shows an underestimation from the theory of the large $\cos\theta^*$ value, especially significant for the central part ($\eta < 1.44$.

Similar discrepancies have already been observed in the diphoton production at hadron colliders [5, 8, 33] and discussed in Ref. [34].

Table 2: Measured cross section of diphoton production as a function of the variable $m_{\gamma\gamma}$ with statistical (stat.) and systematic uncertainties (sys.).

$d\sigma/dm_{\gamma\gamma}$ [pb/ GeV]								
$m_{\gamma\gamma}$ [GeV]	$\lvert\eta\rvert < 1.44$				$\lvert\eta\rvert < 1.44$ or $1.57 < \lvert\eta\rvert < 2.5$			
		stat.	sys.			stat.	sys.	
0−30	0.0299	±0.0071	+0.0069	−0.0086	0.050	±0.013	+0.014	−0.024
30−40	0.061	±0.030	+0.015	−0.018	0.127	±0.049	+0.035	−0.061
40−45	0.097	±0.088	+0.020	−0.020	0.28	±0.17	+0.065	−0.067
45−55	0.77	±0.12	+0.062	−0.054	1.40	±0.20	+0.14	−0.12
55−65	0.705	±0.10	+0.046	−0.039	1.43	±0.18	+0.10	−0.093
65−80	0.408	±0.059	+0.030	−0.031	0.80	±0.11	+0.070	−0.065
80−100	0.175	±0.031	+0.013	−0.012	0.365	±0.063	+0.041	−0.037
100−140	0.070	±0.012	+0.0035	−0.0034	0.142	±0.028	+0.020	−0.018
140−200	0.0102	±0.0035	+6.9E-4	−6.4E-4	0.054	±0.015	+0.0065	−0.0059
200−300	0.0022	±0.0011	+9.8E-5	−8.7E-5	0.0084	±0.0060	+0.0023	−0.0019

Table 3: Measured cross section of diphoton production as a function of the variable $p_{T,\gamma\gamma}$ with statistical (stat.) and systematic uncertainties (sys.).

$d\sigma/dp_{T\gamma\gamma}$ [pb/ GeV]								
$p_{T,\gamma\gamma}$ [GeV]	$\lvert\eta\rvert < 1.44$				$\lvert\eta\rvert < 1.44$ or $1.57 < \lvert\eta\rvert < 2.5$			
		stat.	sys.			stat.	sys.	
0−4	0.93	±0.13	+0.044	−0.047	1.94	±0.32	+0.12	−0.13
4−6	1.20	±0.42	+0.097	−0.085	3.80	±0.88	+0.27	−0.29
6−8	1.68	±0.45	+0.12	−0.12	2.66	±0.87	+0.27	−0.24
8−12	1.24	±0.22	+0.083	−0.076	2.21	±0.45	+0.26	−0.22
12−18	0.85	±0.14	+0.065	−0.062	1.61	±0.28	+0.15	−0.15
18−30	0.320	±0.058	+0.026	−0.022	0.63	±0.12	+0.089	−0.076
30−40	0.262	±0.055	+0.019	−0.017	0.57	±0.10	+0.050	−0.044
40−50	0.234	±0.049	+0.02	−0.019	0.507	±0.093	+0.040	−0.036
50−80	0.077	±0.017	+0.0073	−0.0067	0.153	±0.030	+0.016	−0.016
80−180	0.0084	±0.0026	+6.0E-4	−5.2E-4	0.0150	±0.0036	+0.0010	−8.6E-4

Table 4: Measured cross section of diphoton production as a function of the variable $\Delta\phi_{\gamma\gamma}$ with statistical (stat.) and systematic uncertainties (sys.).

$d\sigma/d\Delta\phi_{\gamma\gamma}$ [pb]								
$\Delta\phi_{\gamma\gamma}$	$\lvert\eta\rvert < 1.44$				$\lvert\eta\rvert < 1.44$ or $1.57 < \lvert\eta\rvert < 2.5$			
		stat.	sys.			stat.	sys.	
$0-\pi/5$	1.87	±0.53	$+0.13$	-0.13	4.65	±0.89	$+0.29$	-0.30
$\pi/5-2\pi/5$	1.77	±0.55	$+0.15$	-0.14	5.5	±1.1	$+0.45$	-0.45
$2\pi/5-3\pi/5$	3.09	±0.72	$+0.31$	-0.29	5.5	±1.3	$+0.61$	-0.54
$3\pi/5-4\pi/5$	7.2	±1.1	$+0.49$	-0.44	16.1	±2.1	$+1.4$	-1.2
$4\pi/5-0.88\pi$	20.8	±2.6	$+1.0$	-0.96	36.7	±5.3	$+3.4$	-3.0
$0.88\pi-0.92\pi$	29.8	±5.1	$+1.7$	-1.5	67	±11	$+5.4$	-5.0
$0.92\pi-0.95\pi$	36.2	±8.1	$+5.1$	-4.7	66	±15	$+8.6$	-7.6
$0.95\pi-0.98\pi$	58.8	±8.8	$+4.2$	-3.8	103	±17	$+12$	-11
$0.98\pi-\pi$	68	±11	$+3.9$	-3.8	141	±23	$+12$	-11

Table 5: Measured cross section of diphoton production as a function of the variable $\cos\theta^*$ with statistical (stat.) and systematic uncertainties (sys.).

$d\sigma/d\cos\theta^*$ [pb]								
$\cos\theta^*$	$\lvert\eta\rvert < 1.44$				$\lvert\eta\rvert < 1.44$ or $1.57 < \lvert\eta\rvert < 2.5$			
		stat.	sys.			stat.	sys.	
$0-0.2$	52.6	±5.2	$+3.1$	-3.2	87.3	±9.0	$+9.1$	-7.9
$0.2-0.4$	38.4	±4.9	$+3.0$	-3.0	67.0	±8.2	$+6.6$	-6.0
$0.4-0.6$	34.8	±4.6	$+2.7$	-2.5	66.0	±7.5	$+5.9$	-5.3
$0.6-0.8$	25.6	±3.7	$+1.6$	-1.5	66.7	±7.7	$+6.1$	-5.3
$0.8-1$	6.4	±1.4	$+0.34$	-0.36	30.8	±7.9	$+5.9$	-4.7

9 Conclusions

The integrated and differential production cross sections of isolated photon pairs have been measured in proton-proton collisions at a centre-of-mass energy of 7 TeV, using data collected by the CMS detector in 2010, corresponding to an integrated luminosity of 36 pb^{-1}. The differential cross sections have been measured as functions of the diphoton invariant mass, the diphoton transverse momentum, the difference of the two photon azimuthal angles, and the $\cos\theta^* = \tanh\frac{y}{2}$ observable. The background contamination from hadron decay products is estimated with a statistical method based on an electromagnetic energy isolation variable $\mathcal{I}$. The signal and background distributions for $\mathcal{I}$ have been entirely extracted from data resulting in systematic uncertainties of approximately 10 % on the measured diphoton yield.

The measurements have been compared to a theoretical prediction performed at next-to-leading-order accuracy using the state-of-the-art fixed order computations [1, 2]. Whereas there is an overall agreement between data and theory for the mass spectrum, the theoretical cross section appears underestimated for regions of the phase space where the two photons are not collinear.

Acknowledgements

We wish to express our gratitude to J-Ph. Guillet, E. Pilon, Z. Bern, L. Dixon, and C. Schmidt for the fruitful discussions on the theoretical aspects concerning the measurement.

We wish to congratulate our colleagues in the CERN accelerator departments for the excellent performance of the LHC machine. We thank the technical and administrative staff at CERN and other CMS institutes, and acknowledge support from: FMSR (Austria); FNRS and FWO (Belgium); CNPq, CAPES, FAPERJ, and FAPESP (Brazil); MES (Bulgaria); CERN; CAS, MoST, and NSFC (China); COLCIENCIAS (Colombia); MSES (Croatia); RPF (Cyprus); Academy of Sciences and NICPB (Estonia); Academy of Finland, MEC, and HIP (Finland); CEA and CNRS/IN2P3 (France); BMBF, DFG, and HGF (Germany); GSRT (Greece); OTKA and NKTH (Hungary); DAE and DST (India); IPM (Iran); SFI (Ireland); INFN (Italy); NRF and WCU (Korea); LAS (Lithuania); CINVESTAV, CONACYT, SEP, and UASLP-FAI (Mexico); MSI (New Zealand); PAEC (Pakistan); SCSR (Poland); FCT (Portugal); JINR (Armenia, Belarus, Georgia, Ukraine, Uzbekistan); MST and MAE (Russia); MSTD (Serbia); MICINN and CPAN (Spain); Swiss Funding Agencies (Switzerland); NSC (Taipei); TUBITAK and TAEK (Turkey); STFC (United Kingdom); DOE and NSF (USA). Individuals have received support from the Marie-Curie programme and the European Research Council (European Union); the Leventis Foundation; the A. P. Sloan Foundation; the Alexander von Humboldt Foundation; the Associazione per lo Sviluppo Scientifico e Tecnologico del Piemonte (Italy); the Belgian Federal Science Policy Office; the Fonds pour la Formation à la Recherche dans l'Industrie et dans l'Agriculture (FRIA-Belgium); the Agentschap voor Innovatie door Wetenschap en Technologie (IWT-Belgium); and the Council of Science and Industrial Research, India.

References

[1] T. Binoth et al., "A full next-to-leading order study of direct photon pair production in hadronic collisions", *Eur. Phys. J.* **C16** (2000) 311, arXiv:hep-ph/9911340. doi:10.1007/s100520050024.

[2] Z. Bern, L. J. Dixon, and C. Schmidt, "Isolating a light Higgs boson from the di-photon background at the LHC", *Phys. Rev.* **D66** (2002) 074018, arXiv:hep-ph/0206194. doi:10.1103/PhysRevD.66.074018.

[3] V. Saleev, "Diphoton production at Tevatron in the quasi-multi-Regge-kinematics approach", *Phys. Rev.* **D80** (2009) 114016, arXiv:0911.5517. doi:10.1103/PhysRevD.80.114016.

[4] C. Balazs et al., "Calculation of prompt diphoton production cross sections at Tevatron and LHC energies", *Phys. Rev.* **D76** (2007) 013009, arXiv:0704.0001. doi:10.1103/PhysRevD.76.013009.

[5] D0 Collaboration, "Measurement of direct photon pair production cross sections in $p\bar{p}$ collisions at $\sqrt{s} = 1.96$ TeV", *Phys. Lett.* **B690** (2010) 108, arXiv:1002.4917. doi:10.1016/j.physletb.2010.05.017.

[6] CDF Collaboration Collaboration, "Measurement of the Cross Section for Prompt Isolated Diphoton Production in $p\bar{p}$ Collisions at $\sqrt{s} = 1.96$ TeV", *Phys. Rev. Lett.* **107** (Sep, 2011) 102003. doi:10.1103/PhysRevLett.107.102003.

[7] CDF Collaboration Collaboration, "Measurement of the cross section for prompt isolated diphoton production in $p\bar{p}$ collisions at $\sqrt{s} = 1.96$ TeV", *Phys. Rev. D* **84** (Sep, 2011) 052006. doi:10.1103/PhysRevD.84.052006.

[8] ATLAS Collaboration, "Measurement of the isolated di-photon cross-section in pp collisions at sqrt(s) = 7 TeV with the ATLAS detector", arXiv:1107.0581.

[9] CMS Collaboration, "The CMS experiment at the CERN LHC", *JINST* **03** (2008) S08004. doi:10.1088/1748-0221/3/08/S08004.

[10] S. Frixione and G. Ridolfi, "Jet photoproduction at HERA", *Nucl. Phys.* **B507** (1997) 315, arXiv:hep-ph/9707345. doi:10.1016/S0550-3213(97)00575-0.

[11] M. Fontannaz, J. Guillet, and G. Heinrich, "Is a large intrinsic k(T) needed to describe photon + jet photoproduction at HERA?", *Eur. Phys. J.* **C22** (2001) 303, arXiv:hep-ph/0107262. doi:10.1007/s100520100797.

[12] T. Sjostrand, S. Mrenna, and P. Skands, "PYTHIA 6.4 Physics and Manual", *JHEP* **05** (2006) 026, arXiv:hep-ph/0603175. doi:10.1088/1126-6708/2006/05/026.

[13] R. Field, "Early LHC Underlying Event Data - Findings and Surprises", *The* PYTHIA6 Z2 *tune is identical to the* Z1 *tune described in this reference, except that* Z2 *uses the* CTEQ6L *PDF while* Z1 *uses* CTEQ5L arXiv:1010.3558.

[14] J. Pumplin, D. Stump, J. Huston et al., "New generation of parton distributions with uncertainties from global QCD analysis", *JHEP* **0207** (2002) 012, arXiv:hep-ph/0201195.

[15] CMS Collaboration, "Photon Reconstruction and Identification at $\sqrt{s} = 7$ TeV", *CMS-PAS-EGM-10-005* (2010).

[16] CMS Collaboration, "Isolated Photon Reconstruction and Identification at $\sqrt{s} = 7$ TeV", *CMS-PAS-EGM-10-006* (2010).

[17] S. Alioli et al., "A general framework for implementing NLO calculations in shower Monte Carlo programs: the POWHEG BOX", *JHEP* **06** (2010) 043, arXiv:1002.2581. doi:10.1007/JHEP06(2010)043.

[18] S. Frixione, P. Nason, and C. Oleari, "Matching NLO QCD computations with Parton Shower simulations: the POWHEG method", *JHEP* **11** (2007) 070, arXiv:0709.2092. doi:10.1088/1126-6708/2007/11/070.

[19] P. Nason, "A new method for combining NLO QCD with shower Monte Carlo algorithms", *JHEP* **11** (2004) 040, arXiv:hep-ph/0409146. doi:10.1088/1126-6708/2004/11/040.

[20] CMS Collaboration Collaboration, "Measurement of the Drell-Yan Cross Section in pp Collisions at sqrt(s) = 7 TeV", arXiv:1108.0566. * Temporary entry *.

[21] M. Pivk and F. R. Le Diberder, "sPlot: a statistical tool to unfold data distributions", *Nucl. Instrum. Meth.* **A555** (2005) 356, arXiv:physics/0402083. doi:10.1016/j.nima.2005.08.106.

[22] CMS Collaboration Collaboration, "Measurements of Inclusive W and Z Cross Sections in pp Collisions at sqrt(s)=7 TeV", *JHEP* **1101** (2011) 080, arXiv:1012.2466. * Temporary entry *. doi:10.1007/JHEP01(2011)080.

[23] CMS Collaboration, "Electron Reconstruction and Identification at $\sqrt{s} = 7$ TeV", *CMS-PAS-EGM-10-004* (2010).

[24] CMS Collaboration, "ECAL 2010 performance results", *CMS Detector Performance Summary* **CMS-DPS-2011-008** (2011).

[25] CMS Collaboration, "Measurement of CMS Luminosity", *CMS-DP-2011-002. Document in preparation* (2011).

[26] L. Bourhis, M. Fontannaz, J. Guillet et al., "Next-to-leading order determination of fragmentation functions", *Eur.Phys.J.* **C19** (2001) 89–98, arXiv:hep-ph/0009101. doi:10.1007/s100520100579.

[27] CDF Collaboration, "Studying the 'underlying event' at CDF and the LHC", *in Proceedings of the First International Workshop on Multiple Partonic Interactions at the LHC MPI08* (2009) 12.

[28] P. Z. Skands, "Tuning Monte Carlo Generators: The Perugia Tunes", *Phys. Rev.* **D82** (2010) 074018, arXiv:1005.3457. doi:10.1103/PhysRevD.82.074018.

[29] M. Botje et al., "The PDF4LHC Working Group Interim Recommendations", arXiv:1101.0538.

[30] H.-L. Lai et al., "New parton distributions for collider physics", *Phys. Rev.* **D82** (2010) 074024, arXiv:1007.2241. doi:10.1103/PhysRevD.82.074024.

[31] A. D. Martin et al., "Parton distributions for the LHC", *Eur. Phys. J.* **C63** (2009) 189, arXiv:0901.0002. doi:10.1140/epjc/s10052-009-1072-5.

[32] R. D. Ball et al., "Impact of Heavy Quark Masses on Parton Distributions and LHC Phenomenology", arXiv:1101.1300.

[33] CDF Collaboration, "Measurement of the Cross Section for Prompt Isolated Diphoton Production in $p\bar{p}$ Collisions at $\sqrt{s} = 1.96 TeV$", arXiv:1106.5123.

[34] T. Binoth et al., "Beyond leading order effects in photon pair production at the Tevatron", *Phys. Rev.* **D63** (2001) 114016, arXiv:hep-ph/0012191. doi:10.1103/PhysRevD.63.114016.